Applied Catalysis B: Environment and Energy 389 (2026) 126597

Contents lists available at ScienceDirect

Applied Catalysis B: Environment and Energy

journal homepage: www.elsevier.com/locate/apcatb

# Synergistic effects of $Ni^{3+}$–$Cu^{0/+}$ dual sites for efficient and stable hydrogen production in AEM water electrolysis

Tao Jiang [a,d,*,1], Ioannis A. Poimenidis [b,1], Dan Luo [a,1], Chongyang Jiang [c], Qingying Zhao [a], Remco Bakker [e], Wanqing Li [a], Marc.C.A. Stuart [f], Paul Arendsen [e], Xiangping Zhang [c], Michalis Konsolakis [b,**], Vasileios Kyriakou [a,**]

[a] Engineering and Technology Institute Groningen (ENTEG), University of Groningen, Nijenborgh 3, Groningen 9747 AG, the Netherlands
[b] Technical University of Crete, School of Production Engineering & Management, Lab of Materials Science and Processes, Crete, Chania 73100, Greece
[c] Beijing Key Laboratory of Ionic Liquids Clean Process, State Key Laboratory of Multiphase Complex Systems, Institute of Process Engineering, Chinese Academy of Sciences, Beijing 100190, China
[d] MESA+ Institute of Nanotechnology, Faculty of Science and Technology, University of Twente, Drienerlolaan 5, Enschede 7522 NB, the Netherlands
[e] Research Institute in Marknesse, Netherlands Aerospace Centre, the Netherlands
[f] Groningen Biomolecular Sciences and Biotechnology Institute, University of Groningen, Nijenborgh 7, Groningen 9747 AG, the Netherlands

ARTICLE INFO

*Keywords:*
$Cu_2O$/NiO heterostructure
Peculiar interfacial charge transfer
Oxygen vacancy
HER kinetics
AEM water electrolysis

ABSTRACT

Achieving efficient and stable hydrogen evolution reaction (HER) with earth-abundant electrocatalysts is pivotal for boosting the efficiency of alkaline water electrolysis. Here, we report an oxygen vacancy ($O_v$)-rich $Cu_2O$/NiO heterostructure, which triggers a peculiar interfacial charge transfer from NiO to $Cu_2O$, creating catalytically active $Ni^{3+}$–$Cu^{0/+}$ dual sites to synergistically promote water dissociation and hydrogen adsorption. The $Cu_2O$/NiO heterostructure exhibits a low overpotential of 19.7 mV at 10 mA $cm^{-2}$ with Tafel slope of 36 mV $dec^{-1}$, outperforming most of the reported catalysts. The anion exchange membrane (AEM) electrolyzer equipped $Cu_2O$/NiO electrode enables 1.78 V to reach 1.0 A $cm^{-2}$ for >200 h of continuous operation. Thorough characterizations including HRTEM/XPS/EPR/XANES and DFT calculations exemplify the interfacial charge transfer dynamics in the $Cu_2O$/NiO heterostructure during HER, offering a new paradigm for rational design of noble metal-free HER electrocatalysts for AEM water electrolysis.

## 1. Introduction

Water electrolysis is a cornerstone technology for green hydrogen production in pursuit of carbon neutrality. [1,2] The hydrogen evolution reaction (HER) taking place at the cathodic electrode is efficiently catalyzed by scarce and expensive platinum in the acidic proton exchange membrane (PEM) electrolyzers[3,4], whereas non-precious Ni-based electrodes are employed in alkaline media. [2,5] Nevertheless, alkaline HER kinetics are more energy-intensive and slower due to the Volmer step (water dissociation), rendering HER critical for the process. [5–7] This challenge has spurred significant efforts for developing earth-abundant electrocatalysts that could rival noble metals in next generation anion exchange membrane (AEM) electrolysis. [8–12]

Strategies to improve alkaline HER generally focus on facilitating the sluggish water dissociation and optimizing hydrogen adsorption. [6,7,13,14] One effective approach is to combine complementary active sites in a heterostructure catalyst to simultaneously accelerate water dissociation (Volmer step) and favor hydrogen adsorption and formation (Heyrovsky/Tafel step). [4,14–17] For instance, interfacing transition metal oxides with metallic Ni or Ni-based alloys have been shown to synergistically promote both reaction steps in alkaline HER. [6,11,12,14,17,18] Similarly, decorating Pt with Ni–Fe hydroxide clusters was shown to improve water adsorption by decreasing the observed overpotentials to ~70 mV at 10 mA $cm^{-2}$, [19] whereas tailoring the orbital orientation in N-doped Pt–Ni alloys pushed the overpotential as low as 15 mV. [20] These studies underscore that interfaces and surface defects

* Corresponding author at:Engineering and Technology Institute Groningen (ENTEG), University of Groningen, Nijenborgh 3, Groningen 9747 AG, the Netherlands.
** Corresponding authors.
*E-mail addresses:* t.jiang@rug.nl (T. Jiang), mkonsolakis@tuc.gr (M. Konsolakis), v.kyriakou@rug.nl (V. Kyriakou).
[1] *The authors contributed equally to this work*

https://doi.org/10.1016/j.apcatb.2026.126597
Received 8 January 2026; Received in revised form 3 February 2026; Accepted 20 February 2026
Available online 21 February 2026

can boost HER activity by altering the reaction energetics, thus offering unique electronic properties due to charge transfer at the interface. The formation of a Mott–Schottky junction can induce an internal electric field that polarizes the interface and enhances adsorption of reaction intermediates, and such interfacial electronic effects provide new active sites and accelerate charge transfer, enabling higher catalytic activity. [4,8,9,16,21] In addition, defect engineering and heterojunction formation have recently been explored to improve alkaline HER. [22–26]

Cu-based electrodes are considered promising for the hydrogen evolution reaction (HER) due to their low cost, abundancy and high electrical conductivity. [13,26–29] In addition, defect engineering of Cu oxides has been shown to enhance the interaction between Cu and intermediates during HER. [26] Specifically, Cu element can weaken the strong hydrogen adsorption energy of Ni oxides/hydroxides to assist hydrogen adsorption/desorption. [30] Hence, Cu-based additives have been reported to modify Ni-based electrodes beneficially for HER. [25, 31–33] However, a challenge for Cu-based electrocatalysts in alkaline media is their susceptibility to oxidation and dissolution. Even when employed as a cathode, it can undergo cathodic corrosion because of oxidation, which significantly undermines its stability. [34–36] Therefore, maintaining its low-valence or metallic state ($Cu^{0/+}$) would be an effective strategy to suppress its dissolution, thus maintaining chemical and structural stability of Cu-based electrodes during alkaline water electrolysis.

On the other hand, the introduction of oxygen vacancies ($O_V$) or other defects in metal oxides alters their electronic structure and can create unsaturated sites that improve catalytic activity. Heterostructured NiO or $Cu_2O$-based catalysts with oxygen vacancies have shown superior performance in related reactions. [22,24,25,37–41] Moreover, oxygen vacancies can enhance the conductivity of NiO by accelerating the transition from p-type into n-type, leading to only 55 mV to deliver 10 mA $cm^{-2}$ in alkaline solutions with good stability. [39] $Cu_2O$-$O_V$ displays a lower energy barrier for the rate-determining step of the water dissociation, thereby accelerating the alkaline HER kinetics. [25]

Inspired by these findings, herein, we have developed an $O_V$-rich $Cu_2O$/NiO heterostructure via simple hydrothermal deposition of NiO in Cu foam (Ni@CF) that exhibits exceptional activity and durability for HER in AEM electrolysis. The formation of $Ni^{3+}$–$Cu^{0/+}$ dual sites and Ov via strong interfacial geometric and electronic interactions, was confirmed by comprehensive characterization including TEM, XPS, EPR, and XAS. These interfacial features collectively induce a built-in electric field and a peculiar charge redistribution, which promotes water dissociation and optimizes hydrogen adsorption energetics. The Ni@CF electrocatalyst exhibits alow overpotential of 19.7 mV at 10 mA $cm^{-2}$ with a Tafel slope of 36 mV $dec^{-1}$ , surpassing the state-of-the-art Pt/C. The electrode was also assembled in a continuous flow AEM electrolyzer with a commercial NiFe LDH anode, in which only 1.78 V was required to achieve 1.0 A $cm^{-2}$ by concurrently demonstrating a remarkable stability for over 200 h at 1.0 A $cm^{-2}$. DFT modeling further revealed that the $Cu_2O$/NiO interface with oxygen vacancies exhibits near-thermoneutral hydrogen adsorption/desorption, which may explain the observed kinetics. Our work provides fundamental insights into how interfacial electronic interactions and defect engineering can be employed to facilitate HER, exemplifying a viable strategy for designing sustainable electrocatalysts toward scalable hydrogen production.

## 2. Experimental section

### 2.1. Materials and chemicals

Ni and Cu foam (XIAMEN TOB NEW ENERGY TECHNOLOGY CO., LTD, China); Pt/C (10 wt%, Alfa Aesar); KOH (90.0 %, Sigma-Aldrich®); $Ni(NO_3)_2{\cdot}6H_2O$ (99.0 %, Sigma-Aldrich®); $Fe(NO_3)_3{\cdot}9\ H_2O$ (98.0 %, Sigma-Aldrich®); urea (99.0 %, Sigma-Aldrich®); NH4F (98.0 %, Sigma-Aldrich®); Nafion (Alfa Aesar); 5 $cm^2$ AEM cell hardware (Dioxide materials); Sustainion® X37–50 Grade 60 Membrane (Dioxide materials).

### 2.2. Preparation of Ni@CF16 and Ni@NF16 electrodes

Hydrothermal method was used to fabricate the Ni@CF16. The Cu foam electrodes (2.5 ×6 $cm^2$) were ultrasonicated for 15 min in pure ethanol. During hydrothermal synthesis, 16 mmol $Ni(NO_3)_2{\cdot}6\ H_2O$ was dissolved under stirring in 80 mL of absolute ethanol. The obtained solution and Cu foam were transferred into a Teflon-lined stainless-steel autoclave and heated at 120 °C for 12 h. Afterward, the copper foam electrodes loaded with the Ni were washed several times with double deionized water and ethanol, dried at 60 °C for 12 h, and finally calcinated at 300 °C for 3 h (heating ramp 5 °C/min) with an air supply. The superiority of Ni@CF16 was demonstrated via a comparison with a series of Ni@CF-X (X = 8, 16, 24) electrodes prepared with the same method, except the concentration (X in mmol) of $Ni(NO_3)_2{\cdot}6\ H_2O$ precursor. Ni@NF16 was synthesized in addition following the same method, except that Ni foam was used instead of Cu foam.

### 2.3. Fabrication of NiFe LDH electrodes

NiFe LDH was directly grown on nickel foam (NF) by hydrothermal process. Firstly, a piece of commercial nickel foam (2.5 ×6 $cm^2$) was cleaned with ethanol, 1 M hydrochloric acid and deionized water in turn for 15 min. Then the NF was rolled into a cylindrical shape and the surface was dried through dust-free paper. Next, 0.218 g of $Ni(NO_3)_2{\cdot}6\ H_2O$, 0.0687 g of $Fe(NO_3)_3{\cdot}9\ H_2O$, 0.36 g urea, and 0.089 g $NH_4F$ were added to 60 mL deionized water and stirred for 30 min. Finally, the solution and NF were transferred to a 100 mL Teflon high-temperature reactor heated at 120 ℃ for 12 h. It was cooled to room temperature, washed with deionized water several times, and dried at 60 ℃ overnight.

### 2.4. Fabrication of Pt/C@NF electrodes

To prepare the Pt/C@NF electrodes, 100 mg Pt/C, 200 μL Nafion, 1 mL ethanol, and 1 mL deionized water were ultrasonicated for 60 min to obtain a homogeneous dispersion. Then, a piece of clean NF (2.5 ×2.5 $cm^2$) was dipped into the dispersion, then dried in air at 333 K for 6 h. The mass loading of the Pt/C catalyst on NF was controlled to be ca. 5.0 mg $cm^{-2}$, as determined by weighing the sample prior to and following the treatment.

### 2.5. Materials characterization

The morphology and elements of the as-prepared samples were characterized by field emission scanning electron microscopy (SEM, Fei NovaNanoSEM 650) and energy dispersive X-ray spectroscopy (EDX) attached to the SEM. The crystal structure was analyzed by X-ray diffraction (XRD, Bruker D8 Endeavor) equipped with a cobalt anticathode (λ=1.78897 Å) and operated at 35 kV, 40 mA. X-ray photoelectron spectroscopy (XPS) using the device of ThermoFisher Nexsa (America) with an Al Kα (λ=1486.6 eV) X-ray source and an energy step of 0.05 eV was conducted to analyze the elemental chemical state of the samples. High-resolution transmission electron microscopy (HR-TEM) images of the catalysts were obtained using a Tecnai T20 electron microscope (FEI) operated at an accelerating voltage of 200 keV. The catalysts were dispersed in ethanol under ultrasonication followed by depositing on a holey carbon-coated copper grid (Quantifoil 1.2/1.3) for measurement. Fast Fourier transforms of high-resolution images were used to check for loss of ordering of the used H-ZSM-5 crystals. Energy Dispersive X-ray (EDX) analyses were performed on an X-Max T80 SDD detector (Oxford Instruments) and are combined with high-angle annular dark field STEM images for both elemental composition and location. Bright-field and high-angle annular dark-field (HAADF) images

were recorded. Distilled water and ethanol were used to clean all the samples before testing commenced thoroughly. JEM-ARM300F was employed to investigate oxygen vacancy under STEM-HAADF mode. UPS Ultraviolet Photoelectron Spectroscopy (Thermo escalab 250Xi) was used for work function measurements.

XAS spectra were measured at the BL14W1 beamlines in Shanghai Synchrotron Radiation Facility (SSRF). The $k^2$-weighted EXAFS data were processed using the ARTEMIS program of the IFEFFIT software codes. EXAFS fitting parameters:

The obtained XAFS data was processed in Athena (version 0.9.26) for background, pre-edge line and post-edge line calibrations. Then Fourier transformed fitting was carried out in Artemis (version 0.9.26). The $k^2$ weighting, k-range of 3–14 $Å^{-1}$ and R range of 1 - ~3 Å were used for the fitting of Ni foil; k-range of 3 – 11.5 $Å^{-1}$ and R range of 1 - ~3 Å were used for the fitting of samples. The four parameters, coordination number, bond length, Debye-Waller factor and $E_0$ shift (CN, R, $\Delta E_0$) were fitted without anyone was fixed, the $\sigma^2$ was set.

Wavelet analysis parameters: For Wavelet Transform analysis, the χ(k) exported from Athena was imported into the Hama Fortran code. The parameters were listed as follow: R range, 1–4 Å, k range, 0–12 $Å^{-1}$ for samples; k weight, 2; and Morlet function with κ= 10, σ= 1 was used as the mother wavelet to provide the overall distribution.

### 2.6. Electrochemical measurements

#### 2.6.1. Half-cell measurements

All electrochemical measurements were carried out using an 8-channel IVIUM-n-Stat Electrochemical Workstation (Module5A/5V-1 MHz) with commercial H-cell test bench, was shown in Figure S8. The H-cell was separated by a commercial anion exchange membrane (AEM, Sustainion® X37–50 Grade 60), which selectively permits $OH^-$ transfer. This configuration effectively prevents the crossover of gas bubbles between the cathode and anode, as well as the migration of dissolved catalyst ions in the electrolyte, thereby eliminating potential interference with the experimental results. The prepared electrodes were used as working electrodes, the Hydrogen Reference Electrode (HRE) (Gaskatel GmbH, Germany) acted as the reference electrode. The HRE was used as the reference electrode and that all reported potentials are referenced to RHE (HRE ≡ RHE under our experimental conditions). The prepared NiFe LDH electrode with an effective size of 1 × 1 $cm^2$ was applied as the counter electrode (CE). Commercial Ni foam (NF), Cu foam (CF), Ni@NF16, Ni@CF16, and precious metal Pt/C electrodes were tested as a comparison under the same conditions. Linear scanning voltammetry (LSV) was performed using a scan rate of 3 mV $s^{-1}$ in 1 M KOH at room temperature. Electrochemical impedance spectra (EIS) were carried out at a frequency range from 100 kHz to 0.1 Hz with an amplitude of 10 mV, at a given potential of –0.3 V vs. RHE toward HER. The double-layer capacitance ($C_{dl}$) values were evaluated from a cyclic voltammogram (CV) method. CV was performed at different scan rates of 20, 60, 100, 140, and 180 mV $s^{-1}$ with a potential range of 0.20 −0.30 V vs. RHE for HER in the non-Faraday region. Therefore, the extracted $C_{dl}$ represents the geometric-area-normalized double-layer capacitance (units: mF·$cm^{-2}$). Consequently, the absolute capacitance is calculated as $C_{dl,\ absolute} = C_{dl} * S$ (1 $cm^2$). Electrochemical active surface area (ECSA) values were calculated from the absolute capacitance ($C_{dl,\ absolute}$) divided by the specific capacitance of an atomically smooth material ($C_{dl}$', ~40 μF $cm^{-2}$) [14]:

$$ECSA = C_{dl,\ absolute}/C_{dl}'$$

$$ECSA\ (Ni@NF16) = C_{dl}/C_{dl}' = 7.35\ mF/40\ \mu F\ cm^{-2} = 18.4\ cm^2$$

$$ECSA\ (Ni@CF16) = C_{dl}/C_{dl}' = 14.89\ mF/40\ \mu F\ cm^{-2} = 37.2\ cm^2$$

This $C_{dl}$' is used to enable relative comparison within the same material system and identical electrolyte/substrate conditions, rather than to claim an absolute surface area with high precision.

### 2.7. AEM electrolyzer cell measurements

A commercial AEM electrolyzer cell driven by an 8-channel IVIUM-n-Stat Electrochemical Workstation (Module 10 A/5V-1 MHz) was employed to examine the performance of the prepared electrodes. Square-shaped 5 $cm^2$ Ni@CF16 electrodes as cathode and NiFe LDH as anode assembled horizontally with Sustainion® X37–50 Grade 60 Membrane as a separator in the commercial AEM electrolyzer cell. Gaskets are made of PTFE, with squared 5 $cm^2$ openings. The cell is made of nickel plates, with channels through which the electrolyte flows on the inner side of the nickel plates, which also serve as the current collectors on each side of the cell. 8 stainless steel fastening bolts are used to secure the final assembly of the electrolyzer. A Digital Torque Screwdriver was used to control the torque applied to the cell. The cells were operated vertically, and 1 M KOH electrolytes were pumped into the cell with a flow rate of 200 mL $min^{-1}$. After 30 min of activation at a constant current of 0.5 A, the cells were characterized by recording I-U curves with a scan rate of 5 mV $s^{-1}$ and the max current up to 10 A. As references, another cell (Ni@NF16(–)||NiFe LDH(+)) with Sustainion® X37–50 Grade 60 Membrane as a separator was also tested under the same conditions. When reporting the current density, this was calculated based on the geometric area of one of the two sides of the foam (the one facing the channels where the electrolyte flows), and thus not considering the contribution of the Ni plate to the activity. This was done for the sake of simplicity and following a common practice in the literature. [42–44] Since the cell configuration is the same in all tests, the calculated current densities allow meaningful comparison of the performance of the different electrodes.

### 2.8. DFT modeling

To investigate the interfacial charge transfer and Gibbs energy of hydrogen formation for $Cu_2O$/NiO heterostructure catalyst, theoretical calculations were carried out using periodic DFT implemented in the Vienna Ab initio Simulation Package (VASP 5.4.4). [45] The projector-augmented method was applied to solve the ion-electron interaction in a periodic system. The generalized gradient approximation with Perdew-Burke-Ernzerh of functionals was used to treat the exchange-correlation interactions in the Kohn-Sham equations. Spin-polarized calculations were carried out with an energy cutoff for the plane waves of 520 eV. The convergence criteria for optimization of the atomic structure were set at 1 × $10^{-5}$ eV and a Hellmann-Feynman force of 0.02 eV Å-1. A Monkforst-Pack k-point mesh of 5 × 5 × 1 k-points was employed. The NiO (012) surface with four atomic layers and 5 × 5 unit cells were used as the model system. To simulate the role of $Cu_2O$ on this heterostructure catalyst, a $Cu_2O$ (220) surface was built. A vacuum layer of 15 Å was added to separate neighboring slabs to avoid possible interaction. The NiO (012) and $Cu_2O$ (220) facets were selected to construct the DFT interface model based on experimental evidence. HRTEM/FFT analyses repeatedly reveal lattice fringes assignable to NiO (012) and $Cu_2O$ (220) at the exposed surface/interface regions, indicating that these planes are among the dominant exposed facets in the $Cu_2O$/NiO heterostructure. Therefore, the DFT model is experiment-guided to reflect the realistic interfacial atomic configuration, rather than assuming equilibrium thermodynamically most stable facets.

## 3. Results and discussion

### 3.1. Preparation and characterization of Ni@CF electrocatalysts

The Ni@CF samples were fabricated via a facile hydrothermal method using Cu foam (CF) as the substrate and different amounts of Ni $(NO_3)_2$·6 $H_2O$ as the NiO precursor for the $Cu_2O$-NiO heterostructure, as illustrated in Fig. 1a (see detailed procedures in the 'Methods' section of the Supporting Information). The as prepared samples are designated as

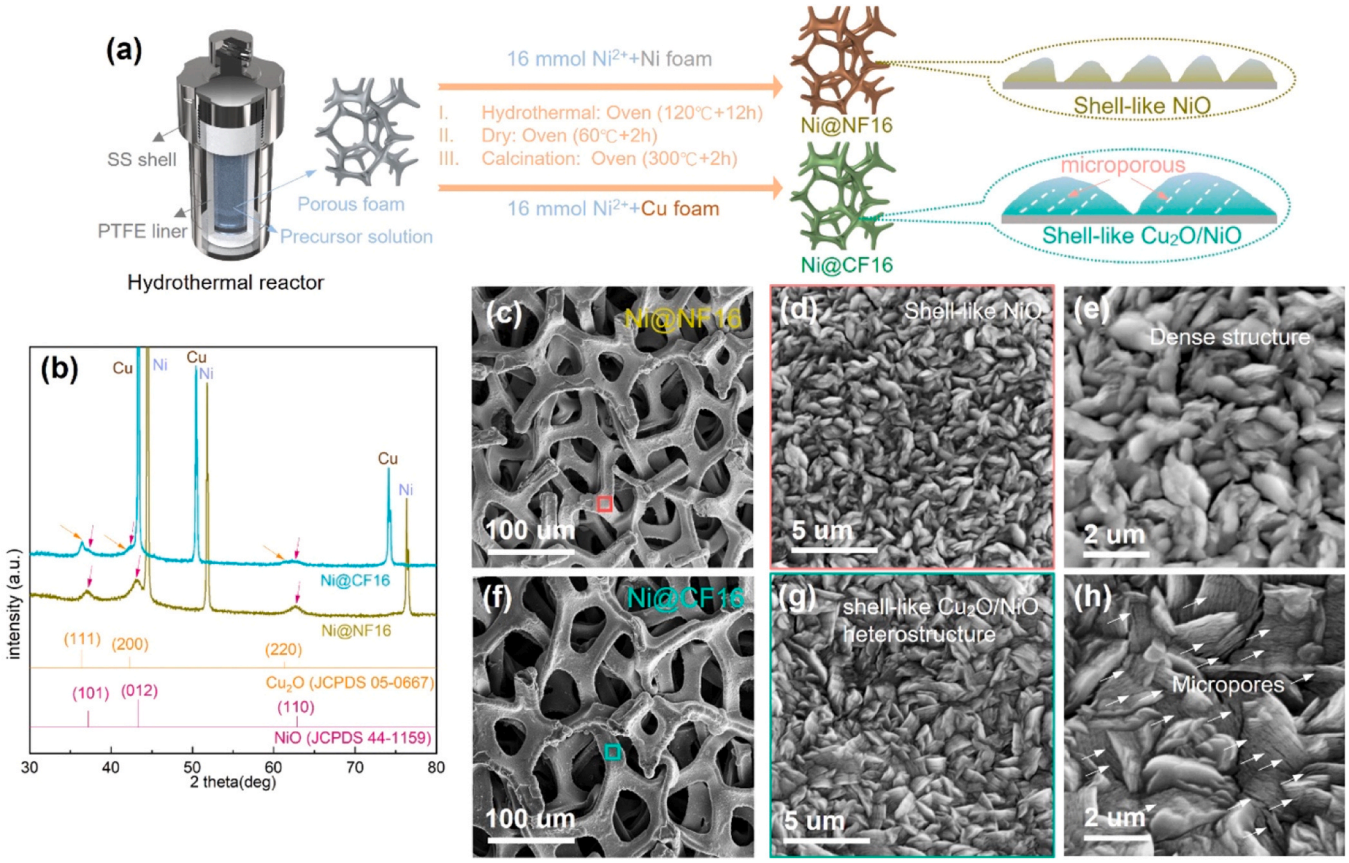


**Fig. 1.** Schematic illustration and physical characterizations of as-prepared electrodes. (a) Schematic illustration of the Ni@CF16 and Ni@NF16 electrodes preparation; (b) XRD patterns of the Ni@NF16 and Ni@CF16 samples; (c-e) typical SEM images from Ni@NF16; (f-h) typical SEM images from Ni@CF16.

Ni@CF-X, where X stands for the concentration (in mmol) of Ni precursor. Herein, a thorough analysis of the optimum sample (Ni@CF16) is provided, whereas information about the remaining samples is included in the Supporting Information. For comparison, pure NiO catalysts supported on Ni foam (Ni@NF16) were prepared using the same procedure, with Cu foam replaced by Ni foam. Following the preparation of the electrodes, X-ray diffraction (XRD) patterns (Fig. 1b) confirm that Ni@NF16 consists of crystalline NiO (indexed to NiO, JCPDS 44–1159), whereas Ni@CF16 displays the NiO phase and additional peaks which correspond to cuprous oxide ($Cu_2O$, JCPDS 05–0667). No peaks of metallic Cu or CuO are detected, indicating that the incorporated Cu is predominantly present as $Cu_2O$ in the as-synthesized catalyst. The presence of $Cu_2O$ alongside NiO in Ni@CF16 suggests the formation of a $Cu_2O$/NiO heterostructure, in agreement with HRTEM results elaborated below.

Scanning electron microscopy (SEM) was performed to analyze the morphological characteristics, which revealed a stark contrast in morphology between Ni@NF16 and Ni@CF16, as shown in Fig. 1(c-h). The NiO layer on Ni@NF16 appears to be relatively dense with a smooth shell-like architecture (Fig. 1(d, e)). In contrast, Ni@CF16 displays a higher porosity (microscale) shell-like architecture composed of interconnected nanoscale flakes and particles (Fig. 1(g, h)). In addition, the surface layer in Ni@CF16 is notably rougher and more tortuous than the compact NiO layer in Ni@NF16, which should enhance electrolyte permeability and gas diffusion. SEM-EDS (Figure S1) analysis confirmed the uniform distribution of Ni, Cu, and O elements in Ni@CF16, further indicating that both $Cu_2O$ and NiO phases were homogeneously dispersed throughout the structure.

Transmission electron microscopy (TEM) was carried out to characterize the structures for Ni@NF16 electrocatalysts and the results are shown in Figure S2. The TEM image of Ni@NF16 (Figure S2a) revealed densely packed NiO nanocrystals with well-defined grain boundaries. The crystallites are ~5 nm in size, possessing more grain boundaries. The selected area electron diffraction (SAED) pattern of Ni@NF16 in Figure S2b, exhibits sharp diffraction rings indexed to NiO (JCPDS 44–1159), confirming the polycrystalline nature of the NiO phase with well-aligned lattice domains. High-resolution TEM (HRTEM) image (Figure S2c) of NiO from Ni@NF16 shows clear lattice fringes with an interplanar spacing of ~0.208 nm, corresponding to the (012) plane of NiO, indicating good crystallinity.

TEM and STEM-HAADF (High-angle annular dark-field) were conducted to further analysis Ni@CF16 structures, as shown in Fig. 2. Notably, the average nanocrystal size in the sample Ni@CF16 is about 10 nm, as shown in Fig. 2a, which is approximately double to that of Ni@NF16. The increased grain size in the $Cu_2O$/NiO heterostructure for Ni@CF16 can be attributed to nickel–copper interactions that promote recrystallization and reduce surface energy, thereby facilitating grain growth. [46] Besides typically being more stable (lower surface energy), structures with the larger crystallites are also more conductive due to the lower number of grain boundaries [47], [48] The NiO-only Ni@NF16 also contains numerous grain boundaries that could impede electron flow and serve as dissolution/vacancy diffusion paths, potentially limiting its long-term stability.

In contrast, the Ni@CF16 larger crystals and coherent $Cu_2O$/NiO interface (observed as lattice continuity at the junctions in HRTEM) suggest a robust structure with good electrical percolation. HRTEM of Ni@CF16 (Fig. 2b) shows distinct lattice fringes with two types of interplanar spacings: ~0.208 nm (NiO (012)) and ~0.152 nm ($Cu_2O$ (220)). The clear interface between these regions highlights the intimate contact between the two oxides. Such a heterojunction would facilitate the interfacial charge transfer, promoting the formation of $Ni^{3+}$ and $Cu^{0/+}$ dual sites. Fast Fourier transform (FFT) of the HRTEM image (Fig. 2c)

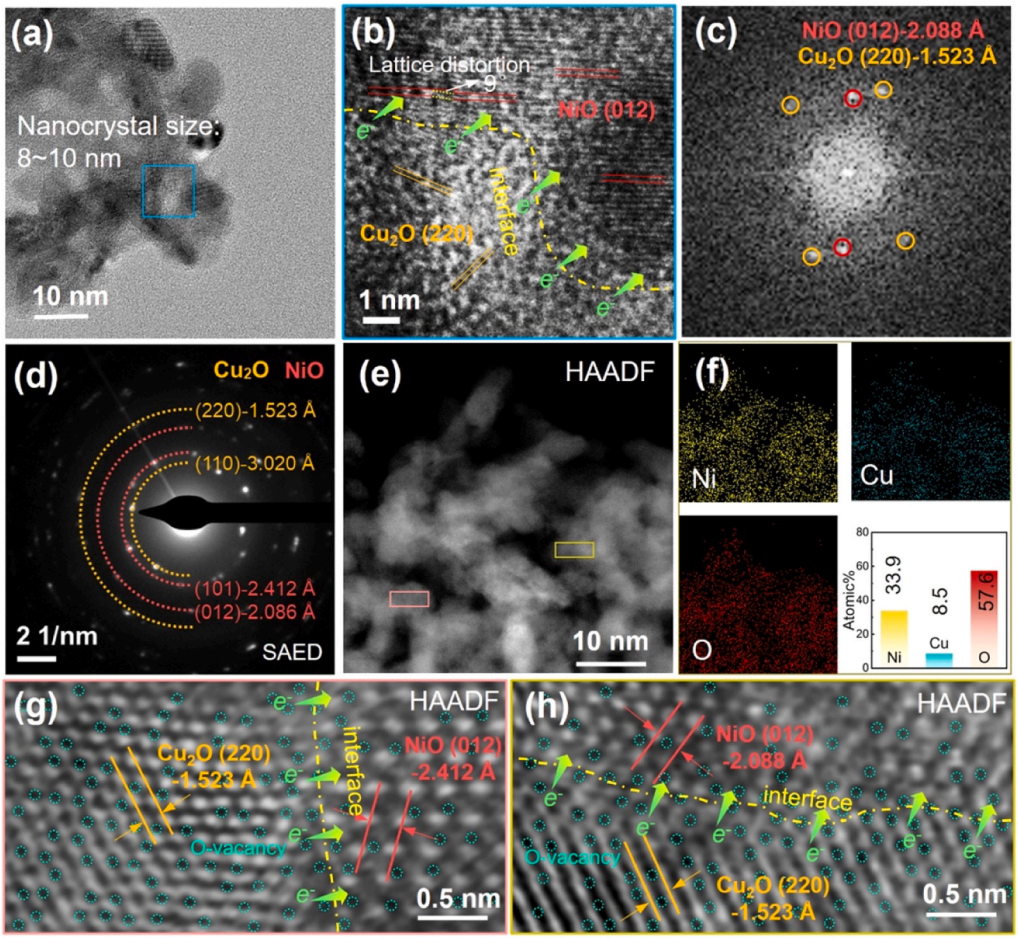


**Fig. 2.** TEM and STEM analysis of the $Cu_2O$/NiO heterostructure in Ni@CF16 electrodes. (a) TEM image; (b) Lattice image of $Cu_2O$/NiO heterostructure; (c) FFT of $Cu_2O$/NiO interface lattices from Fig. 2(b); (d) SAED pattern of $Cu_2O$/NiO heterostructure; (e) STEM-HAADF image of $Cu_2O$/NiO heterostructure; (f) Ni, Cu, and O elements distribution and atomic ratio of $Cu_2O$/NiO from Fig. 2(e); (g and h) STEM-HAADF atomic images of O-vacancies and $Cu_2O$/NiO interfaces from Fig. 2(e).

further verifies the coexistence of two crystalline domains with different zone axes, corresponding to NiO and $Cu_2O$. The well-aligned lattice fringes and sharp FFT spots indicate coherent interfacial bonding, which is vital for maintaining electronic coupling and structural stability under HER conditions. Fig. 2d displays the SAED pattern of Ni@CF16, which shows additional diffraction rings beyond those of NiO, corresponding to $Cu_2O$ (JCPDS 05–0667). The coexistence of NiO and $Cu_2O$ rings confirms the successful formation of a $Cu_2O$/NiO heterostructure, which is critical for enabling interfacial electronic modulation and dual-site HER catalysis. Fig. 2(e–f) exhibits HAADF-STEM image and elemental mapping of Ni@CF16, confirming homogeneous dispersion of Ni, Cu, and O. The uniform overlap of all three elements supports the formation of a nanoscale $Cu_2O$/NiO heterostructure, ensuring uniform catalytic behavior across the electrode surface. High-resolution atomic images in Fig. 2(g–h) further reveal the $Cu_2O$/NiO interfacial regions, where abundant oxygen vacancies are observed within $Cu_2O$ and at the $Cu_2O$/NiO interfaces.

To gain insights into the oxidation states and structural features of the $Cu_2O$/NiO heterostructure, a combination of X-ray Photoelectron Spectroscopy (XPS), Electron Paramagnetic Resonance (EPR), and X-ray Absorption Spectroscopy (XAS) analyses were performed. The Ni 2p XPS spectra in Fig. 3a reveal a notable shift and broadening in the Ni@CF16 sample compared to Ni@NF16. The main Ni $2p_{3/2}$ peak in Ni@CF16 is shifted to slightly higher binding energy (~855.7 eV), and a satellite peak emerges more prominently, indicating an increased number of high-valence $Ni^{3+}$ species. [49] This implies interfacial charge transfer in the $Cu_2O$/NiO heterostructure; $Cu_2O$ coupling oxidizes some $Ni^{2+}$ to $Ni^{3+}$ (holes in NiO or Ni–O–Cu bonds) to maintain charge balance. UPS was conducted to measure work function values for Ni@NF16 and Ni@CF16 samples, as shown in Figure S3. The work function for NiO (Ni@NF16) and $Cu_2O$/NiO heterostructure (Ni@CF16) were detected with the values are 4.67 eV, 4.91 eV, respectively. The higher work function of the $Cu_2O$/NiO heterostructure indicates a downward shift of the Fermi level. Although we cannot measure $Cu_2O$ alone under identical conditions, the observed increase in work function upon forming the heterostructure supports the scenario that $Cu_2O$ possesses a higher intrinsic work function than NiO, manifesting electron transfer from NiO to $Cu_2O$. This observation is in agreement with our XPS results, where Ni 2p features exhibit positive shifts. The generation of $Ni^{3+}$ (more electron-deficient Ni centers) is significant because these sites are highly electrophilic and can strongly attract $OH^-$ from water dissociation, promoting faster Volmer-step kinetics for HER. [50] In essence, the Ni 2p XPS confirms an in-situ formed high-valent Ni phase at the interface, which correlates with improved water adsorption/dissociation and thus, enhanced HER activity on Ni@CF16.

Cu 2p XPS spectra of Ni@CF16 (Fig. 3b) show distinct peaks for $Cu^+$ and $Cu^0$ states at ~932.5 eV, along with weak satellite structures at higher binding energies, indicating only a trace presence of $Cu^{2+}$. [25, 51] To unambiguously determine the oxidation states of Cu in the $Cu_2O$/NiO heterostructure, Cu LMM Auger spectroscopy was further conducted. As shown in Figure S4, Ni@CF16 exhibits two well-resolved Auger features corresponding to $Cu^+$ and $Cu^0$, whose kinetic-energy positions agree well with the established Cu LMM reference values. Quantitative peak deconvolution reveals that the as-prepared sample

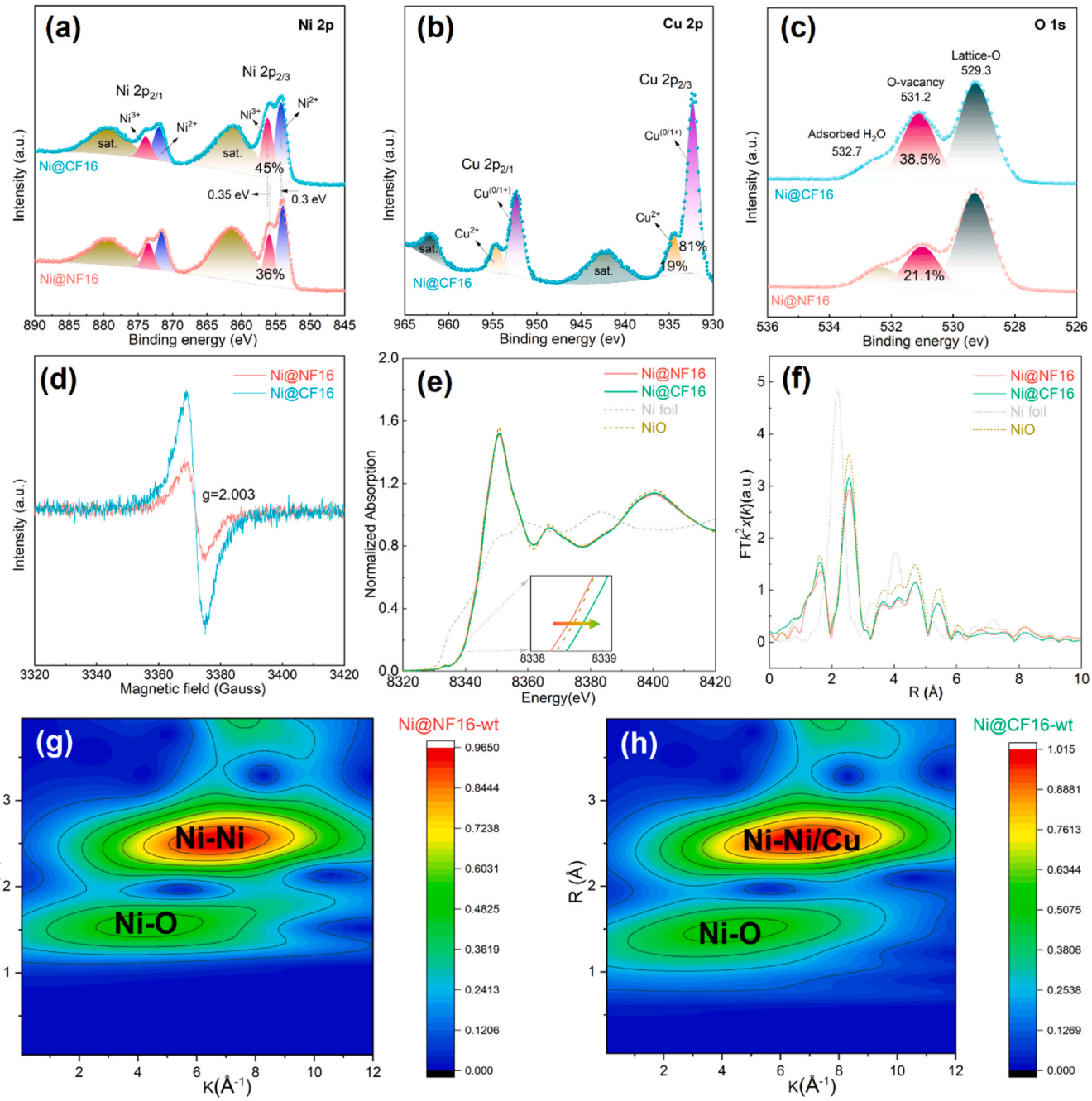


**Fig. 3.** Chemical state and atomic coordination of NiO and $Cu_2O$/NiO heterostructure over Ni@NF16 and Ni@CF16 electrodes. (a) High-resolution XPS spectra for Ni 2p; (b) High-resolution XPS spectra for Cu 2p; (c) High-resolution XPS spectra for O 1 s; (d) EPR analysis of oxygen vacancy for NiO in Ni@NF16 and $Cu_2O$/NiO heterostructure in Ni@CF16; (e) XANES Ni K-edge spectra; (f) FT curves of Ni foil, NiO, Ni@NF16 and Ni@CF16; (g) EXAFS wavelet transform plots of NiO in Ni@NF16; (h) EXAFS wavelet transform plots of $Cu_2O$/NiO in Ni@CF16.

contains 54.7 % $Cu^0$ and 45.3 % $Cu^+$, confirming the coexistence of metallic and cuprous species within the heterostructure. This mixed valence ($Cu^{0/+}$) environment is consistent with reduced copper domains stabilized within the heterostructure, providing conductive, H-affinitive sites: Cu metal/$Cu^+$ sites bind hydrogen intermediates moderately and facilitate electron transfer. Such $Cu^0$/$Cu^+$ species at the interface complement NiO by optimally adsorbing hydrogen and facilitating its desorption, thereby accelerating the later HER steps (hydrogen adsorption–desorption) in synergy with the water-splitting capability of NiO. Thus, the coexistence of oxidized Ni and reduced Cu confirms the peculiar interfacial charge redistribution, which would accelerate water dissociation and hydrogen adsorption in alkaline HER. [4,15,16] Notably, the $Cu^0$ component revealed by XPS/Auger is primarily attributed to the partial reduction of $Cu^+$ species within the $Cu_2O$ phase at the $Cu_2O$/NiO interface. This reduction is driven by interfacial charge redistribution and oxygen-vacancy formation, rather than by bulk metallic Cu from the foam substrate. While a minor contribution from the Cu foam cannot be fully excluded, its influence on the surface-sensitive spectra is expected to be negligible. Although isolated $Cu_2O$ is known to be metastable under ambient conditions, the $Cu_2O$ species observed here are stabilized by strong interfacial coupling with NiO. The Cu valence states were therefore identified based on combined Cu 2p and Cu LMM Auger analyses, rather than assuming ideal bulk $Cu_2O$ stability.

The O 1 s XPS spectra (Fig. 3c) exhibit two main components: a low binding energy peak at ~529.3 eV attributed to lattice oxygen ($O^{2-}$ in metal oxides), and a higher binding energy shoulder (~531.2 eV) corresponding to oxygen vacancies or surface hydroxyls. The latter feature is markedly enhanced in Ni@CF16, suggesting a higher oxygen vacancy concentration at the $Cu_2O$/NiO interface, which create unsaturated Ni–O coordination and localized charges that can enhance HER kinetics: oxygen vacancies increase the metal–oxygen covalency and facilitate water molecule adsorption and dissociation. [22] In the Volmer step, water can more easily adsorb and split at vacancy-rich sites (providing $OH^-$ to fill the vacancy and adsorbed hydrogen to the metal), so the enriched defect density in Ni@CF16 directly contributes to faster hydrogen generation. O 1 s deconvolution is not used to assign vacancies, instead, it only complements the STEM observations.

Moreover, the EPR results (Fig. 3d) provide clear evidence of unpaired electrons (paramagnetic centers) in the catalysts. Ni@CF16 displays a pronounced EPR signal with $g \approx 2.003$, whereas Ni@NF16 shows a very weak/no signal. A g~2.0 resonance is characteristic of electrons trapped in oxygen vacancies (F-centers) or $Ni^{3+}$ ($d^7$) high-spin sites. [52] The strong EPR signal in Ni@CF16 thus confirms the creation of ample oxygen vacancies and/or $Ni^{3+}$ centers in the $Cu_2O$/NiO heterostructure (in agreement with the XPS observations). These paramagnetic defects indicate a richer electronic state and a partially reduced oxide surface for Ni@CF16. Functionally, the presence of oxygen-vacancy sites and high-valent Ni centers boosts HER: oxygen vacancies act as active sites for water activation, stabilizing the adsorption of $OH^-$ and facilitating its removal, while $Ni^{3+}$ can polarize water molecules more effectively. [50] Consequently, the EPR evidence of more Ni@CF16 defects correlates with a catalyst surface that more readily undergoes the Volmer reaction and binds hydrogen intermediates, thereby expediting HER kinetics. EPR signal serves only as supportive evidence in combination with STEM results.

The Ni K-edge XANES spectra were conducted to compare the unoccupied electronic structure of Ni in both samples (Fig. 3e). Ni@CF16 shows a slight edge energy shift upward and an intensified white-line (absorption peak) relative to Ni@NF16, indicating a higher Ni oxidation state in the heterostructure. In NiO from the Ni@NF16 sample, Ni is ~2 +, while in Ni@CF16 the XANES edge position moves closer toward $Ni^{3+}$ reference values, consistent with the XPS-detected $Ni^{3+}$ species. This edge shift and whiteline growth indicate that interfacial Ni atoms have an elevated valence (approaching $Ni^{3+}$) due to $Cu_2O$–NiO electronic interactions. The formation of $Ni^{3+}$ (holes in Ni 3d states) at the $Cu_2O$/NiO interface is a strong electronic modifier: higher-valent Ni cations have more covalency with oxygen and a stronger affinity for hydroxide. [50] Thus, the XANES confirms an altered Ni coordination/electronic structure in Ni@CF16 consistent with $Ni^{3+}$ and oxygen-defect generation. These $Ni^{3+}$ centers at the interface are directly tied to HER enhancement (they improve the adsorption of $OH^-$) and adjust the d-band of Ni to optimize hydrogen binding energy, ultimately speeding up adsorbed hydrogen formation and subsequent $H_2$ release.

The Fourier-transformed EXAFS (extended X-ray absorption fine structure) (Fig. 3f, Figure S6, and Table S1) provide real-space insight into the Ni local environment. For Ni@NF16, the FT-EXAFS shows a strong first-shell Ni–O peak at ~1.6 Å (phase-uncorrected) and a significant second-shell Ni–Ni peak near ~2.7 Å, matching the NiO crystal structure (each $Ni^{2+}$ is coordinated by $O^{2-}$ and neighboring $Ni^{2+}$ in the lattice). In Ni@CF16, these features are notably altered: the Ni–O peak is attenuated or slightly shifted, and the Ni–Ni coordination peak is significantly reduced in intensity (and potentially shifted) compared to Ni@NF16. The dampening of the Ni–Ni EXAFS signal implies that many Ni sites in Ni@CF16 have fewer Ni neighbors, which is consistent with NiO lattice disruption by oxygen vacancies and the presence of Cu at the interface. The Ni–O coordination number decrease (or shorter Ni–O bonds) corroborates oxygen-deficient NiO (vacancies cause missing O neighbors and/or a slight contraction of Ni–O distance due to higher oxidation state). Meanwhile, new scattering contributions from Ni–Cu bonds may arise, although they overlap in radius with Ni–Ni and their presence is supported by the overall modified amplitude.

These structural changes suggest an interfacial reorganization: Ni@CF16 contains defective Ni, Cu-coupled coordination environment, unlike the pristine NiO in Ni@NF16. Such an environment is expected to be beneficial for HER, fewer Ni–Ni bonds and more Ni–$O_v$ or Ni–Cu bonds mean more unsaturated catalytic sites and adjusted metal–metal interactions, which can lower energy barriers for H adsorption/desorption. [25,53] In particular, oxygen vacancies and Ni–Cu bonding can modulate the local electron density of Ni, facilitating water dissociation (Volmer step) and tuning hydrogen binding energy to an optimum, thereby accelerating HER kinetics.

The wavelet transforms EXAFS (Fig. 3g and Figure S7) acts as a 2D fingerprint of backscattering atom types for Ni in Ni@NF16 (NiO). It shows two main intensity regions: one at low R (~1.5 Å) and lower k, corresponding to Ni–O interactions (light O scatterers yield maxima at lower k), and another at higher R (~2.8–3.0 Å) and intermediate k (~7–8 $Å^{-1}$) arising from Ni–Ni scattering in the NiO lattice. [54] Hence, the WT plot for Ni@NF16 shows that the first-shell O neighbors and second-shell Ni neighbors for Ni, with no indication of heavier scatterers since NiO contains no elements heavier than Ni. This serves as a baseline confirming that Ni@NF16 is a stoichiometric NiO structure without foreign atoms or significant vacancies, which would otherwise alter the intensity distribution. The lack of additional features means Ni@NF16 provides a stable but less active environment with Ni–O and Ni–Ni alone (as in bulk NiO) are not optimal for HER, since pure NiO offers limited H adsorption sites and electronic conductivity.

On the other hand, the WT-EXAFS of Ni@CF16 (Fig. 3h) exhibits a distinctly different second-shell pattern compared to Ni@NF16, highlighting the structural impact of the $Cu_2O$/NiO heterostructure. The Ni–O first-shell signal at low R and low k is preserved, indicating that Ni remains primarily coordinated with oxygen. Notably, the second-shell wavelet intensity in Ni@CF16 shifts toward a higher k region (~8–9 $Å^{-1}$) relative to Ni@NF16. [54] Such a shift toward higher k values is characteristic of a heavier backscattering atom and is therefore indicative of altered second-neighbor environments around Ni. Considering the presence of Cu in the heterostructure and the close similarity in Ni–Ni and Ni–Cu scattering distances, this feature is reasonably attributed to interfacial Ni–Cu interactions, rather than solely Ni–Ni coordination as in pristine NiO.

It should be emphasized that WT-EXAFS provides qualitative, element-sensitive insight into the local coordination environment. While the similarity of backscattering amplitudes and the limited signal-to-noise ratio prevent a statistically robust, independent quantification of a Ni–Cu path in conventional EXAFS fitting, the observed k-shift in the wavelet map offers strong indicative evidence for Ni–Cu coupling at the $Cu_2O$/NiO interface. The emergence of such interfacial Ni–Cu coordination, together with the reduced contribution from Ni–Ni scattering and the presence of oxygen vacancies, suggests a vacancy-rich and electronically perturbed NiO lattice intimately coupled with $Cu_2O$. This atomic-scale integration is consistent with the enhanced HER performance of Ni@CF16, where interfacial Ni sites (including $Ni^{3+}$/vacancy-associated motifs) facilitate water dissociation, while adjacent $Cu^{0}$/$^{+}$ sites favor balanced hydrogen adsorption and $H_2$ evolution. [50] Collectively, the WT-EXAFS analysis supports the role of interfacial electronic and structural synergy, rather than a single structural parameter, in governing the improved HER kinetics.

### 3.2. *Electrocatalytic HER activity and AEM water electrolysis performance*

The HER performance of Ni@CF16 and Ni@NF16 was first evaluated in a three-electrode H-cell configuration (Figure S8) in 1.0 M KOH. Fig. 4a compares the polarization curves of Ni@CF16 ($Cu_2O$/NiO) and Ni@NF16 (NiO) for the hydrogen evolution reaction (HER) in 1.0 M KOH. For comparison purposes, the corresponding performance of bare

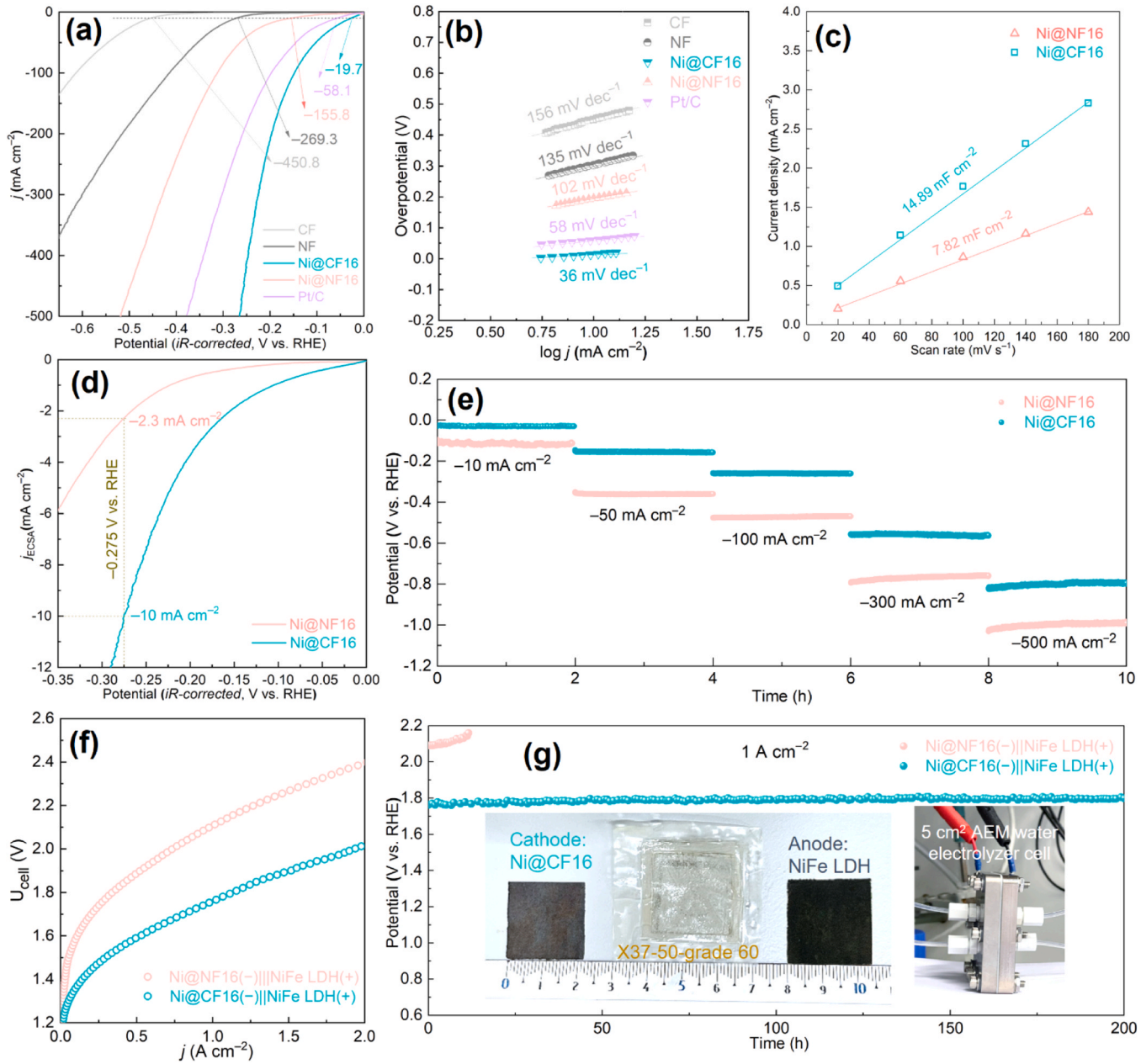


**Fig. 4.** Electrocatalytic HER activity and AEM Water Electrolysis Performance. (a) LSV curves for HER; (b) Corresponding Tafel plots for HER; (c) $C_{dl}$ for Ni@NF16 and Ni@CF16 electrodes; (d) LSV curves based on the ECSA normalized current densities for HER; (e) Stability test at different current densities for Ni@NF16 and Ni@CF16 electrodes; (f) Polarization curves for AEM water electrolyzer cells with various electrodes at 60°C; (g) The long-term operation stability at 1 A $cm^{-2}$ for AEM water electrolyzer cells at 60°C.

NF and CF as well as of noble-metal based Pt/C is included. Ni@CF16 exhibits a markedly enhanced HER activity, evidenced by a much earlier onset of cathodic current and significantly higher current densities at any given overpotential compared to Ni@NF16. In practical terms, Ni@CF16 requires an ultralow overpotential of 19.7 mV to reach 10 mA $cm^{-2}$, while the values are 58.1 and 155.8 mV for noble-metal based Pt/C and Ni@NF16, respectively. The corresponding values for the bare CF are much higher, clearly revealing the synergistic effects imposed by Ni-Cu interactions. In addition, LSV curves for Ni@CF8 and Ni@CF32 were also investigated, which also display lower overpotentials of 25.3 and 43.5 mV (Figure S9) respectively, even when compared to state-of-the-art noble metal-based systems. XPS analysis of the Ni 2p, Cu 2p and O 1 s spectra for Ni@CF8 and Ni@CF32 samples was also conducted (Figure S5). The proportions of $Ni^{3+}$ and $Cu^{0/+}$ species were found to be 41 % and 59 % for Ni@CF8, and 42 % and 67 % for Ni@CF32, respectively. In comparison, Ni@CF16 exhibited higher ratios of 45 % $Ni^{3+}$ and 81 % $Cu^{0/+}$, further confirming that Ni@CF16 possesses a greater abundance of $Ni^{3+}$–$Cu^{0/+}$ active sites. In addition, XPS semi-quantitative analysis reveals surface Cu/Ni ratios of 35.01/2.45 (Ni@CF8), 32.17/2.70 (Ni@CF16), and 32.62/3.37 (Ni@CF32), indicating that Ni@CF16 possesses a more balanced Cu/Ni composition, whereas Ni@CF8 is Cu-rich and Ni@CF32 is Ni-rich. The corresponding O-vacancy fractions are 33.2 %, 37.5 %, and 32.6 %, respectively, with Ni@CF16 exhibiting the highest vacancy concentration. These results suggest that an optimal Cu/Ni ratio (as in Ni@CF16) promotes oxygen-vacancy formation and stabilizes interfacial $Ni^{3+}/Cu^{0}$ species, thereby enhancing electronic reconstruction at the $Cu_2O$/NiO interface and contributing to the superior HER activity of Ni@CF16. Fig. 4b presents the Tafel plots derived from the LSV data, highlighting the HER kinetic slope for Ni@CF16. Ni@CF16 exhibits a significantly

smaller Tafel slope of 36 mV $dec^{-1}$ , compared to Pt/C (58 mV $dec^{-1}$) and Ni@NF16 (102 mV $dec^{-1}$). The fact that the slope of Ni@CF16 is much lower than that of Ni@NF16 signifies that the surface of Ni@CF16 dramatically accelerates the initial water-splitting step due to the presence of $Ni^{3+}$ centers, as discussed previously. Concurrently, adjacent $Cu^{0/+}$ sites on Ni@CF16 can readily accept the hydrogen intermediate, aiding its rapid recombination into molecular $H_2$. Thus, the Tafel analysis here supports that the interface design ($Cu_2O$/NiO heterostructure with oxygen vacancies) of Ni@CF16 leads to a more kinetically favorable HER pathway, evidencing faster reaction rates per decade of current increase compared to the NiO-only catalyst. [18,55]

Double-layer capacitances ($C_{dl}$) calculated from different-scan-rate CV curves (Figure S10) for Ni@CF16 and Ni@CF16 were shown in Fig. 4c. Ni@CF16, incorporating the $Cu_2O$/NiO heterostructure, exhibits double the $C_{dl}$, compared to pure NiO from Ni@NF16. This increased surface capacitance is most likely correlated to the rougher shell-like structures observed in the SEM images. Fig. 4d compares the HER polarization curves normalized by the electrochemical active surface area (ECSA) for Ni@CF16 (49.7 $cm^2$) and Ni@NF16 (24.5 $cm^2$). Even after normalizing for ECSA (i.e. comparing intrinsic activity per active site), Ni@CF16 still delivers higher current densities at equivalent overpotentials than Ni@NF16. This indicates that, beyond having a higher surface area, the Ni@CF16 catalyst possesses intrinsically higher activity of sites. The interfacial electronic modulation in the $Cu_2O$/NiO composite could be critical in this aspect. The coupling of NiO with $Cu_2O$ (and metallic Cu) alters the electronic structure of Ni and Cu at their interface, tuning the binding energies of reaction intermediates to optimal levels. In a similar manner, the introduction of Cu into Ni-based catalysts has been shown to induce a higher Ni valence state and create heterogeneous interfaces, which could be related to hydrogen adsorption and charge transfer. [56] In Ni@CF16, XPS/XAS characterizations indeed reveal a portion of $Ni^{3+}$ and the presence of oxygen vacancies, indicating an electronically rich surface. These features may increase the intrinsic reactivity of each site, with $Ni^{3+}$ species to effectively interact with water/$OH^-$, while $Cu^{0/+}$ to stabilize adsorbed hydrogen, resulting in greater HER currents per active site.

On the other hand, oxygen vacancies in Ni@CF16 are also expected to contribute to the higher intrinsic activity by improving electrical conductivity and providing unsaturated coordination sites. Oxygen-deficient NiO has been shown to exhibit enhanced charge-transfer and even stronger $H_2O$ adsorption affinity than stoichiometric NiO. [56] Thus, the ECSA-normalized curves confirm that the performance advantage of Ni@CF16 is not merely due to more surface area, but could be related to $Ni^{\delta+}$–$Cu^{\delta-}$ dual sites and $O_V$ defects that synergistically boost the HER reaction on a per-site basis. Electrochemical impedance spectroscopy (EIS) was performed to evaluate the charge transfer resistance of all samples, as shown in Figure S11 and Table S2. The results indicate that Ni@CF16 with $Cu_2O$/NiO heterostructures exhibits the lowest charge transfer resistance (0.35 Ohm $cm^2$) towards HER, compared with Pt/C (0.51 Ohm $cm^2$), Ni@NF16 (1.27 Ohm $cm^2$), NF (2.26 Ohm $cm^2$), and CF (17.24 Ohm $cm^2$). Fig. 4e illustrates the short-term stability of Ni@CF16 at different constant current densities of 10, 50, 100, 300, and 500 mA·$cm^{-2}$. Ni@CF16 demonstrates adequate stability across all tested current densities, maintaining a low potential over prolonged operation at each step. Notably, even at high current densities, the potential of Ni@CF16 only shows a stabilization period during the first minutes, indicating a promising catalyst durability. By contrast, the Ni@NF16 reference either requires a higher initial potential to sustain the same currents or shows a more rapid rise in potential. The superior stability of Ni@CF16 can be linked to its unique composition and defect structure discussed above. Specifically, Ni–$O_v$–Cu interface in Ni@CF16 may suppress the agglomeration or detachment of active NiO species that pure NiO/Ni foam electrodes suffer under gas-evolving conditions. Furthermore, the presence of Cu in the material can improve corrosion resistance and mechanical integrity of the catalyst layer. [57] Oxygen vacancies might also contribute to stability since vacancies could accommodate local lattice strain during redox cycling and prevent the formation of insulating $Ni(OH)_2$ layers. Lastly, the $Ni^{3+}$–$Cu^{0/+}$ dual active sites could enable a self-regulating surface state, i.e., during operation, $Ni^{2+} \leftrightarrow Ni^{3+}$ redox transitions (involving lattice oxygen or $OH^-$) and $Cu^{0/+}$ transitions might occur that maintain an optimal catalytic phase without permanent degradation. Such charge-driven formation of active Ni states not only enhances $H_2O$ adsorption and Volmer reaction kinetics but also mimics electronic metal–support interaction (EMSI) reported in reducible oxide-supported catalysts, such as CuO–$CeO_2$, where the support modulates the metal electronic structure. [58,59] However, unlike traditional EMSI involving a passive oxide support, the $Cu_2O$/NiO system forms a conductive bimetallic interface that enables bidirectional electronic coupling and generates bifunctional active sites via the redox equilibrium $Ni^{2+} + Cu^+ \leftrightarrow Ni^{3+} + Cu^0$. To the best of our knowledge, this is the first report on hydrothermally-induced metal oxide – metal foam interfacial charge transfer leading to the formation of highly efficient $Ni^{\delta+}/Cu^{\delta-}$ redox pairs. This dual mechanism extends classical EMSI by incorporating geometric coordination and dynamic electron exchange in a metallic heterostructure, potentially offering higher intrinsic activity and stability for alkaline HER.

The HER activity of the Ni@CF16 was compared with the leading HER catalysts reported, as shown in Table S3. The obtained HER activity exceeds most of the state-of-the-art catalysts reported. Moreover, its simple composition and facile preparation method further enhance its effectiveness as a platinum-free HER electrocatalyst for practical AEM water electrolysis. To demonstrate the practical applicability of the HER catalyst, it was assembled in a 5 $cm^2$ AEM water electrolyzer cell. The cell used Ni@CF16 or Ni@NF16 as the cathode (HER catalyst), NiFe LDH sample as anode, and an X37–50-grade 60 type anion exchange membrane separating the electrodes. The electrolyzer was operated with 1.0 M KOH at 60 ℃. Fig. 4f depicts the received polarization curves with Ni@CF16 or Ni@NF16 as the cathode (HER catalyst). The Ni@CF16-equipped AEM cell delivers lower cell voltages at all current densities relative to the cell with Ni@NF16, demonstrating substantially improved overall water splitting efficiency. Specifically, at a high current density of 1 A $cm^{-2}$, the Ni@CF16 cell only requires cell voltage of 1.78 V, whereas the Ni@NF16 cell requires a significantly higher voltage (2.09 V) to sustain the same current. The polarization curves validate that the materials innovations in Ni@CF16 (dual active sites and defect-engineered interface) confer a meaningful advantage at the device level, enabling higher current densities at lower cell voltage facilitating hydrogen production.

Fig. 4g highlights the long-term durability of the AEM water electrolyzer constructed with Ni@CF16 operating at a constant current density of 1 A $cm^{-2}$. The plot displays the cell voltage as a function of continuous operation time at this high current density. With Ni@CF16, the cell voltage remains low and relatively stable over 200 h, indicating excellent durability under heavy-duty operating conditions. Any rise in cell voltage over time is minimal, suggesting that Ni@CF16 suffers little performance loss or catalyst degradation throughout the test. However, the AEM electrolyzer equipped Ni@NF16 exhibits a severe degradation in cell performance after 12 h of operation under 1.0 A $cm^{-2}$. The robust durability of Ni@CF16 in the AEM cell stems from the same structural and chemical attributes that enhanced its half-cell stability. The Ni–Cu heterostructured catalyst likely resists common degradation mechanisms in alkaline electrolysis, such as catalyst deactivation, delamination, or Ostwald ripening. Cu incorporation can mitigate oxidation of the nickel catalyst under the bipolar conditions of a full cell (where the cathode experiences high $H_2$ coverage and the anode generates $O_2$). Moreover, the interfacial electronic modulation in Ni@CF16 may also play a protective role. The charge redistribution between Ni, Cu, and oxygen vacancies can circumvent harmful surface reactions. For instance, in Ni-Cu-Ov systems, the Ni lattice has been shown to be electronically buffered by oxygen vacancies, which suppresses excessive hydrogen binding and ultimately limits Ni corrosion. [60] Finally, the

porous structure in Ni@CF16 electrode most likely promotes swift gas release, preventing local pressure buildup or blocking of active sites by $H_2$ bubbles, thereby maintaining performance.

Overall, the observed durability combined with its low overpotential, exemplifies that Ni@CF16 is a highly active and stable HER catalyst for practical alkaline AEM electrolyzers. The structure and morphology of Ni@CF16 remained well-preserved after a 200-h stability test at an industrially relevant current density of 1 A $cm^{-2}$, as evidenced by XRD (Figure S12) and SEM-EDS analysis (Figure S13). Wrinkled ripple flakes were observed on the Ni@CF16-HER sample, due to the continuous large amount of $H_2$ bubble generation and desorption from the surface of the sample. Notably, XPS results (Figure S14) revealed an increased proportion of $Ni^{3+}$ and $Cu^{0/+}$ species in the post-test sample compared to the pristine one, further indicating that the $Ni^{3+}$–$Cu^{0/+}$ dual active sites synergistically contribute to the efficient and stable hydrogen evolution. Interestingly, metallic Ni was identified in the Ni@CF16-HER sample, offering additional active sites that synergize with $Cu^{0/+}$ species to enhance hydrogen adsorption. [11,14] These findings collectively confirm the excellent electrochemical durability of the Ni@CF16 electrode.

### 3.3. HER mechanism in $Cu_2O$/NiO heterostructures

To further understand the underlying mechanism of HER in such heterostructures, density functional theory (DFT) calculations were carried out (Fig. 5). The experimentally verified $Cu_2O$/NiO heterostructure in Ni@CF16, rich in interfacial oxygen vacancies (as confirmed by TEM, XPS, EPR, and XAS), and the pure NiO counterpart in Ni@NF16 were modeled accordingly. Based on these findings, representative models of $Cu_2O$/NiO with oxygen vacancies ($Cu_2O$/NiO-$O_V$) and pristine NiO were constructed. For comparison, additional models of $Cu_2O$/NiO without oxygen vacancies and pure $Cu_2O$ were also developed to discern the individual and synergistic contributions of each component and the role of interfacial defects. Fig. 5a illustrates the charge density difference for $Cu_2O$/NiO-$O_V$ from Ni@CF16 compared to the isolated NiO and $Cu_2O$ components. Regions of electron accumulation (shown in yellow) and depletion (cyan) highlight a significant redistribution of charge at the junction. Notably, a pronounced build-up of electron density appears at the interface, indicating that electrons are transferred across the junction. Moreover, a 0.59 electron migration from NiO into $Cu_2O$ was calculated, which was consistent with the results of XPS analysis in prior studies where Ni in NiO is partially oxidized (emergence of $Ni^{3+}$ species) upon interfacing with $Cu_2O$. This implies that electrons migrate from NiO to $Cu_2O$, leaving electron-deficient Ni sites ($Ni^{2+} \rightarrow Ni^{3+}$), while enriching Cu sites ($Cu^{1+} \rightarrow Cu^{0/+}$) at the interface. Such peculiar interfacial charge transfer with NiO acting as an electron donor despite typically being a p-type oxide is probably driven by the alignment of Fermi levels and is exacerbated by structural defects. In particular, oxygen vacancies can play a crucial role since oxygen-deficient NiO contains excess electrons that are readily donated to the adjacent $Cu_2O$, further increasing electron density at the interface. [25] This also leads to the formation of a built-in electric field oriented from NiO to $Cu_2O$. This internal field and charge-polarized interface (electron-rich $Cu_2O$ side vs. electron-poor NiO side) validates the strong interfacial electronic coupling. Such charge redistribution is expected to modify adsorption properties at the interface, creating unique active sites distinct from those on either pure $Cu_2O$, NiO, and $Cu_2O$/NiO.

The HER pathway in alkaline media involves two main stages: water dissociation, and hydrogen adsorption/desorption. [14,29] The free energy diagram for the proposed HER pathways on the surface of NiO (Ni@CF16), $Cu_2O$, $Cu_2O$/NiO, and $Cu_2O$/NiO-$O_V$ (Ni@CF16) catalysts is proposed in Fig. 5b. The water dissociation energies of NiO (Ni@CF16), $Cu_2O$, $Cu_2O$/NiO, and $Cu_2O$/NiO-$O_V$ (Ni@CF16) catalysts are calculated to be 1.53, 2.16, 0.95, and 0.10 eV, respectively. The $Cu_2O$/NiO-$O_V$ (Ni@CF16) catalyst exhibits the lowest free energy of 0.10 eV (very close to zero) for water dissociation, attributed to the emergence of $Ni^{3+}$ species in $Cu_2O$/NiO-$O_V$ (Ni@CF16) catalyst. For the hydrogen adsorption/desorption process, the $Cu_2O$/NiO-$O_V$ interface also yields a Gibbs free energy very close to zero (–0.11 eV), whereas NiO, $Cu_2O$, and $Cu_2O$/NiO exhibit less favorable values (deviating positively or negatively from zero). According to the Sabatier principle, an ideal HER catalyst binds hydrogen neither too weakly nor too strongly – quantitatively, Gibbs free energy for hydrogen adsorption/desorption should be ~0 eV for optimal activity. [61] Thus, the near-zero Gibbs free energy at the $Cu_2O$/NiO-$O_V$ interface indicates an almost optimal hydrogen binding energy, which is a key contributor to faster HER kinetics. [62] In contrast, hydrogen adsorption on NiO, $Cu_2O$, or $Cu_2O$/NiO is thermodynamically less optimal (either endergonic, indicating too weak hydrogen binding, or too exergonic, indicating overly strong binding). The modulated interface in $Cu_2O$/NiO-$O_V$ effectively balances these two extremes, achieving a sweet spot where adsorbed hydrogen can form and release efficiently. This thermoneutral hydrogen adsorption/desorption suggests that hydrogen intermediates can readily attach and detach at the interface, avoiding kinetic bottlenecks in the Volmer–Heyrovsky/Tafel steps. Consequently, the $O_V$-rich $Cu_2O$/NiO heterojunction should exhibit markedly improved HER activity, consistent

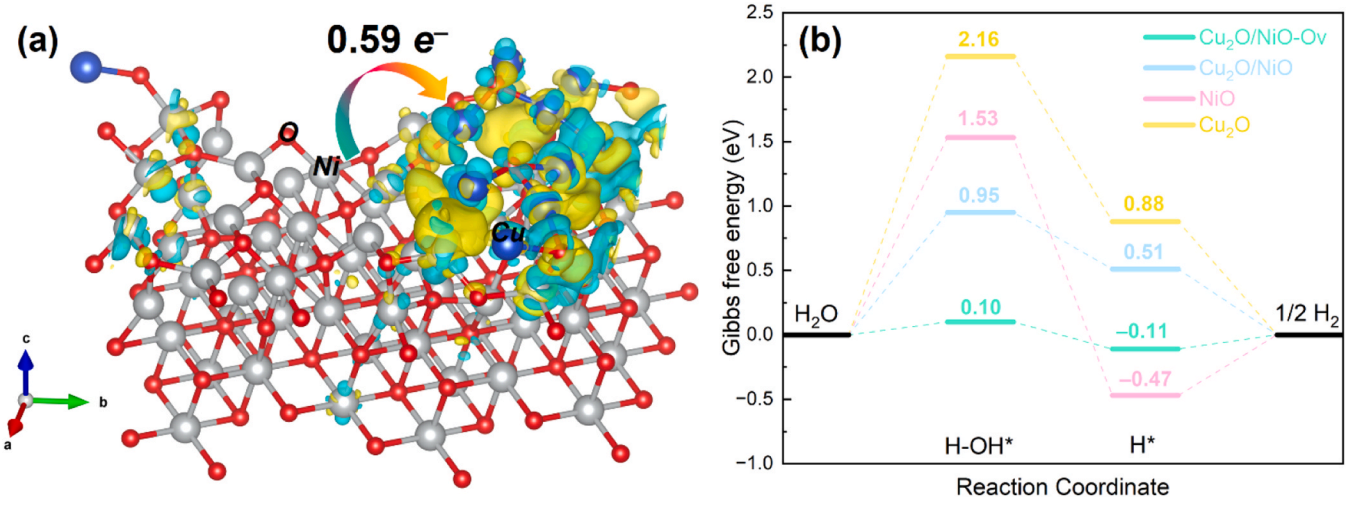


**Fig. 5.** DFT calculations of interfacial charge transfer and Gibbs energy of hydrogen formation for various electrodes. (a) The 3D charge density difference of heterostructured $Cu_2O$/NiO-$O_V$ from Ni@CF16 electrode; (b) The calculated free energy diagrams for different HER pathways on $Cu_2O$/NiO-$O_V$ (Ni@CF16), $Cu_2O$/NiO, NiO (Ni@NF16) and $Cu_2O$ electrodes.

with the experimental observation of accelerated $H_2$ evolution on this composite catalyst (Ni@CF16).

The DFT findings point to a dual active-site mechanism at the $O_V$ engineering $Cu_2O$/NiO interface that underpins this optimal behavior. In the heterostructure, adjacent Cu and Ni sites assume complementary roles in the HER. The interfacial Cu atoms – partially reduced to $Cu^0$ (or $Cu^+$ with elevated electron density) provide hydrogen-binding sites that adsorb hydrogen moderately, preventing overly strong metal–hydrogen bonds. Meanwhile, the neighboring Ni atoms, which can be even oxidized to an unusually high valence ($Ni^{3+}$) due to interfacial electron depletion, serve as oxophilic sites that readily interact with water and hydroxide. These $Ni^{3+}$ centers can effectively cleave H–OH bonds by stabilizing the OH* fragment (forming Ni–OH bonds) and thus, facilitate water dissociation (the Volmer step). Simultaneously, the $Cu^{0/+}$ sites bind the hydrogen atom (H*) resulting from water splitting just strongly enough to enable subsequent recombination or electron transfer to form $H_2$. This synergistic effect means that each half-reaction is optimized on different sites, with the $Ni^{3+}$ site lowering the barrier for $H_2O$ activation (producing abundant H* and OH*), and the Cu site providing a favorable platform for H* adsorption/desorption and H–H coupling. In the present system, the $Ni^{3+}$– $Cu^{0/+}$ dual active sites at the $Cu_2O$/NiO junction allow independent tuning of the OH* and H* binding affinities, optimizing both water dissociation and hydrogen adsorption/desorption steps.

## 4. Conclusion

In summary, we have developed an $O_V$-rich $Cu_2O$/NiO heterostructured catalyst that achieves exceptional HER performance. The material is synthesized in-situ on a Cu foam to create a self-supported electrode (denoted as Ni@CF16) via a simple hydrothermal process, whereas a Cu-free NiO on Ni foam (Ni@NF16) was prepared for benchmarking. We demonstrate that $Cu_2O$ incorporation fundamentally transforms the NiO catalyst with the Ni@CF16 to develop a unique micro/nano-porous shell morphology (in contrast to the dense NiO film of Ni@NF16) that exhibits a high density of oxygen vacancies at the NiO-$Cu_2O$ interface. In addition, the NiO crystallite size in Ni@CF16 (10 nm) is about twice that of Ni@NF16 (5 nm), which partially mitigate grain-boundary corrosion and enhance stability. EPR and XPS reveal a high number of oxygen vacancies and a high $Ni^{3+}$ oxidation state in Ni@CF16, indicating an electron transfer from NiO to $Cu_2O$, which results in an internal electric field across the junction as confirmed by the DFT calculations. This interfacial charge redistribution involves NiO (normally a poor HER conductor) with highly active surface Ni sites ($Ni^{3+}$) for water dissociation and electron-rich Cu sites for optimal hydrogen adsorption. Moreover, the relatively low valence state of $Cu^{0/+}$ is maintained, limiting corrosion and dissolution of Cu, thereby ensuring long-term stability. Benefiting from these multi-faceted advantages, the Ni@CF16 catalyst exhibits a HER overpotential of just 19.7 mV at 10 mA $cm^{-2}$, with a Tafel slope of 36 mV $dec^{-1}$ indicating fast Volmer–Heyrovsky kinetics. By introducing Ni@CF16 as the cathode in an AEM electrolyzer, 1.0 A $cm^{-2}$ was achieved at 1.78 V of cell voltage and 60 °C of temperature for 200 h. Our findings reveal that under cathodic HER conditions, the $Cu_2O$/NiO heterostructure undergoes selective interfacial reconstruction rather than complete reduction. $Cu_2O$ is partially reduced to interfacial $Cu^0/Cu^+$ species, whereas NiO remains in an oxidized, defect-rich state with stabilized $Ni^{3+}$ centers. The resulting $Ni^{3+}$–$Cu^0/^+$ dual active sites constitute the true catalytically operative ensemble, synergistically promoting water dissociation and optimizing hydrogen adsorption/desorption. This dynamic dual-site mechanism highlights a promising design strategy for low-cost, high-performance water-splitting electrodes in AEM electrolyzers.

## CRediT authorship contribution statement

T.J., I.A.P., and D.L. designed and performed the experimental work. T.J. and D.L. carried out the physicochemical characterizations and analysis, HER/AEM cell performance tests/analysis. T.J. led every stage from initial conceptualization to drafting/refining the manuscript. C.Y. J. performed the DFT modeling. D.L., Q.Y.Z., W.Q.L., and R.B. supported the electrode preparation. M.C.A.S. provided support on TEM analysis. X.P.Z. supported DFT modeling. P.A. provided critical suggestions for the strategy of the experimental work. M.K. and V.K. conceptualized the research, supported the design of the experimental work, and secured the funding. All authors discussed the results and edited the manuscript.

## Declaration of Competing Interest

The authors declare that they have no known competing financial interests or personal relationships that could have appeared to influence the work reported in this paper.

## Acknowledgments

The authors would like to acknowledge the financial support by the Nederlands Lucht- en Ruimtevaartcentrum (NLR).

## Appendix A. Supporting information

Supplementary data associated with this article can be found in the online version at doi:10.1016/j.apcatb.2026.126597.

## Data Availability

Data will be made available on request.

## References

[1] J. Du, Z. Li, L. Wang, Y. Ding, W. Ye, W. Yang, L. Sun, Anion exchange membrane seawater electrolysis at 1.0 A cm(-2) with an anode catalyst stable for 9000H, Adv. Sci. (2025) 2416661.
[2] A.A. Feidenhans'l, Y.N. Regmi, C. Wei, D. Xia, J. Kibsgaard, L.A. King, Precious metal free hydrogen evolution catalyst design and application, Chem. Rev. 124 (2024) 5617–5667.
[3] L.L. Wang, X.R. Wang, H.J. Wang, C. Zhang, J.J. Li, G.J. Feng, X.X. Cheng, X. R. Qin, Z.Y. Yu, T.B. Lu, Tailoring Lewis acidity of metal oxides on nickel to boost electrocatalytic hydrogen evolution in neutral electrolyte, J. Am. Chem. Soc. 147 (2025) 7555–7563.
[4] H. Huang, L. Xu, S. Zuo, Y. Ren, L. Song, C. Zou, X. Wang, J.R. Martinez, K. W. Huang, H. Zhang, Pioneering built-in interfacial electric field for enhanced anion exchange membrane water electrolysis, Angew. Chem. Int. Ed. Engl. 64 (2025) e202414647.
[5] T. Kou, Chen, M., Wu, F., Smart, T.J., Wang, S., Wu, Y., … & Li, Y., Carbon doping switching on the hydrogen adsorption activity of NiO for hydrogen evolution reaction, Nat. Commun., 11 590.
[6] Z.J. Chen, G.X. Cao, L.Y. Gan, H. Dai, N. Xu, M.J. Zang, P. Wang, Highly dispersed platinum on honeycomb-like NiO@ Ni film as a synergistic electrocatalyst for the hydrogen evolution reaction, ACS Catal. 8 (2018) 8866–8872.
[7] C. Han, C. Cheng, W. Lv, L. Xiao, J. Zhang, Y. Zhao, Za Ma, Z. Liu, J. Wang, Q. Yun, R. Zhang, C. Dong, H. Liu, P.F. Yin, X.W. Du, J. Yang, Hydrogen spillover enabled by edge dislocations for efficient hydrogen evolution, Adv. Funct. Mater. (2025).
[8] L. Yang, H. Liu, Y. Li, L. Zhong, Z. Jin, X. Xu, D. Cao, Z. Chen, Customizing bonding affinity with multi-intermediates via interfacial electron capture to boost hydrogen evolution in alkaline water electrolysis, Angew. Chem. Int. Ed. Engl. 64 (2025) e202414518.
[9] L. Yi, K. Nie, B. Li, Y. Zhang, C. Hu, X. Hao, Z. Wang, X. Qu, Z. Liu, W. Huang, Tailoring copper single-atoms-stabilized metastable transition-metal-dichalcogenides for sustainable hydrogen production, Angew. Chem. Int. Ed. Engl. 64 (2025) e202414701.
[10] D.D. Alemayehu, M.C. Tsai, M.H. Tsai, C.C. Yang, C.C. Chang, C.Y. Chang, E. A. Moges, K. Lakshmanan, Y. Nikodimos, W.N. Su, C.H. Wang, B.J. Hwang, Heterogeneous Interfaces of Ni(3)Se(4) Nanoclusters Decorated on a Ni(3)N surface enhance efficient and durable hydrogen evolution reactions in alkaline electrolyte, J. Am. Chem. Soc. 147 (2025) 16047–16059.
[11] I.O. Baibars, H. Huang, Y. Xiao, S. Wang, Y. Nie, C. Jia, K. Dastafkan, C. Zhao, Efficient hydrogen evolution at Ni/CeOx interfaces in anion-exchange membrane water electrolysers, Energy Environ. Sci. (2025).
[12] A. Dong, G. Lin, Z. Li, W. Wu, X. Cao, W. Li, L. Wang, Y. Zhao, D. Chen, L. Sun, Interlayer-bonded Ni/MoO(2) electrocatalyst for efficient hydrogen evolution reaction with stability over 6000h at 1000 mA cm(-2), Nat. Commun. 16 (2025) 4955.
[13] C. Yang, W. Zhong, K. Shen, Q. Zhang, R. Zhao, H. Xiang, J. Wu, X. Li, N. Yang, Electrochemically Reconstructed Cu-FeOOH/$Fe_3O_4$ catalyst for efficient hydrogen evolution in alkaline media, Adv. Energy Mater. 12 (2022) 2200077.

[14] N.I. Kim, J. Lee, S. Jin, J. Jeong, S.W. Myeong, J.S. Ha, J. Park, H. Lee, M. Park, C. Kim, S. Kim, S.H. Yang, Y.S. Park, J. Lee, J.Y. Lee, M.H. Seo, S.M. Choi, Collapsing the bottleneck by interfacial effect of Ni/CeO(2) for long-term hydrogen production using waste alkaline water in practical-scale anion exchange membrane water electrolyzer, Adv. Sci. (Weinh. ) (2025) e02484.
[15] J. Huang, J. Han, T. Wu, K. Feng, T. Yao, X. Wang, S. Liu, J. Zhong, Z. Zhang, Y. Zhang, B. Song, Boosting hydrogen transfer during volmer reaction at oxides/metal nanocomposites for efficient alkaline hydrogen evolution, ACS Energy Lett. 4 (2019) 3002–3010.
[16] K. Lu, Y. Liu, F. Lin, I.A. Cordova, S. Gao, B. Li, B. Peng, H. Xu, J. Kaelin, D. Coliz, C. Wang, Y. Shao, Y. Cheng, Li(x)NiO/Ni heterostructure with strong basic lattice oxygen enables electrocatalytic hydrogen evolution with pt-like activity, J. Am. Chem. Soc. 142 (2020) 12613–12619.
[17] G. Lin, A. Dong, Z. Li, W. Li, X. Cao, Y. Zhao, L. Wang, L. Sun, An Interlayer Anchored NiMo/MoO(2) electrocatalyst for hydrogen evolution reaction in anion exchange membrane water electrolysis at high current density, Adv. Mater. (2025) e2507525.
[18] L. Zhao, Y. Zhang, Z. Zhao, Q.H. Zhang, L.B. Huang, L. Gu, G. Lu, J.S. Hu, L.J. Wan, Steering elementary steps towards efficient alkaline hydrogen evolution via size-dependent Ni/NiO nanoscale heterosurfaces, Natl. Sci. Rev. 7 (2020) 27–36.
[19] G. Shi, T. Tano, D.A. Tryk, A. Iiyama, M. Uchida, K. Terao, H. Osada, M. Yamaguchi, K. Tamoto, K. Kakinuma, Nanostructured Pt-nife oxide catalyst for hydrogen evolution reaction in alkaline electrolyte membrane water electrolyzers, ACS Catal. 14 (2024) 9460–9468.
[20] J. Yang, J. Wang, R. Hübner, X. Tao, Y. Ren, Z. Zheng, W. Liu, Highly open phosphorized ptni nanohexapod/N-doped graphene aerogel for high-performance alkaline hydrogen evolution, Adv. Energy Mater. 15 (2024) 2404684.
[21] J.Y. Zhang, J. Liang, B. Mei, K. Lan, L. Zu, T. Zhao, Y. Ma, Y. Chen, Z. Lv, Y. Yang, C. Yu, Z. Xu, B.Y. Xia, W. Li, Q. Yuan, D. Zhao, Synthesis of Ni/NiO@MoO3−x composite nanoarrays for high current density hydrogen evolution reaction, Adv. Energy Mater. 12 (2022) 2200001.
[22] T. Zhang, M.-Y. Wu, D.-Y. Yan, J. Mao, H. Liu, W.-B. Hu, X.-W. Du, T. Ling, S.-Z. Qiao, Engineering oxygen vacancy on NiO nanorod arrays for alkaline hydrogen evolution, Nano Energy 43 (2018) 103–109.
[23] F. Zhang, R. Ji, Y. Liu, Z. Li, Z. Liu, S. Lu, Y. Wang, X. Wu, H. Jin, B. Cai, Defect-rich engineering and F dopant Co-modulated NiO hollow dendritic skeleton as a self-supported electrode for high-current density hydrogen evolution reaction, Chem. Eng. J. 401 (2020) 126037.
[24] Y. Yan, J. Lin, T. Xu, B. Liu, K. Huang, L. Qiao, S. Liu, J. Cao, S.C. Jun, Y. Yamauchi, J. Qi, Atomic-level platinum filling into Ni-Vacancies of Dual-Deficient NiO for boosting electrocatalytic hydrogen evolution, Adv. Energy Mater. 12 (2022) 2200434.
[25] J. Ren, Q. Wang, Q. Xiang, C. Yang, Y. Liang, J. Li, J. Liu, D. Qian, O-vacancy-rich and heterostructured Cu/Cu2O/NiO@NiCu foam self-supported advanced electrocatalyst towards hydrogen evolution: an experimental and DFT study, Chem. Eng. Sci. 280 (2023) 119026.
[26] Z. Li, Y. Wang, H. Liu, Y. Feng, X. Du, Z. Xie, J. Zhou, Y. Liu, Y. Song, F. Wang, M. Sui, Y. Lu, F. Fang, D. Sun, Electroreduction-driven distorted nanotwins activate pure Cu for efficient hydrogen evolution, Nat. Mater. 24 (2025) 424–432.
[27] K. Chung, J. Bang, A. Thacharon, H.Y. Song, S.H. Kang, W.S. Jang, N. Dhull, D. Thapa, C.M. Ajmal, B. Song, S.G. Lee, Z. Wang, A. Jetybayeva, S. Hong, K.H. Lee, E.J. Cho, S. Baik, S.H. Oh, Y.M. Kim, Y.H. Lee, S.G. Kim, S.W. Kim, Non-oxidized bare copper nanoparticles with surface excess electrons in air, Nat. Nanotechnol. 17 (2022) 285–291.
[28] S.J. Kim, Y.I. Kim, B. Lamichhane, Y.H. Kim, Y. Lee, C.R. Cho, M. Cheon, J.C. Kim, H.Y. Jeong, T. Ha, J. Kim, Y.H. Lee, S.G. Kim, Y.M. Kim, S.Y. Jeong, Flat-surface-assisted and self-regulated oxidation resistance of Cu(111), Nature 603 (2022) 434–438.
[29] M. Jiang, J. Xu, Q. Zhou, Y. Chen, P. Munroe, L. Li, Z.H. Xie, Y. Wu, S. Peng, Rationally Designed Asymmetric Pt-O-Cu ligand to stabilize active sites towards superior industrial-standard alkaline hydrogen evolution, Angew. Chem. Int. Ed. Engl. (2025) e202510259.
[30] J. Wang, S. Xin, Y. Xiao, Z. Zhang, Z. Li, W. Zhang, C. Li, R. Bao, J. Peng, J. Yi, S. Chou, Manipulating the water dissociation electrocatalytic sites of bimetallic nickel-based alloys for highly efficient alkaline hydrogen evolution, Angew. Chem. Int. Ed. Engl. 61 (2022) e202202518.
[31] C. Cheng, F. Chen, B. Zhang, B.H. Zhao, X. Du, Promoting water dissociation and weakening active hydrogen adsorption to boost the hydrogen transfer reaction over a Cu-Ag superlattice electrocatalyst, Angew. Chem. Int. Ed. Engl. 64 (2025) e202413897.
[32] Y. Feng, X. Lv, H. Wang, H. Wang, F. Yan, L. Wang, H. Wang, J.T. Ren, Z.Y. Yuan, *H species regulation of heterostructured Cu2O/NiO nanoflowers boosting tandem nitrite reduction for high-efficiency ammonia production, Adv. Funct. Mater. (2025).
[33] Y. Wan, W. Wei, S. Ding, L. Wu, H. Qin, X. Yuan, A multi-site synergistic effect in high-entropy alloy for efficient hydrogen evolution, Adv. Funct. Mater. 35 (2024) 2414554.
[34] M.Y. Gao, C. Yang, Q.B. Zhang, Y.W. Yu, Y.X. Hua, Y. Li, P. Dong, Electrochemical fabrication of porous Ni-Cu alloy nanosheets with high catalytic activity for hydrogen evolution, Electrochim. Acta 215 (2016) 609–616.
[35] S. Liu, Y. Li, D. Wang, S. Xi, H. Xu, Y. Wang, X. Li, W. Zang, W. Liu, M. Su, K. Yan, A.C. Nielander, A.B. Wong, J. Lu, T.F. Jaramillo, L. Wang, P. Canepa, Q. He, Alkali cation-induced cathodic corrosion in Cu electrocatalysts, Nat. Commun. 15 (2024) 5080.
[36] H.P. Sarker, A. Goswami, M.T. Tang, F. Abild-Pedersen, From Micro-environments to macroscopic effects: how the alkaline hydrogen evolution reaction drives Cu Cathodic Corrosion, ACS Catal. (2025) 8676–8690.
[37] H. Zhong, G. Gao, X. Wang, H. Wu, S. Shen, W. Zuo, G. Cai, G. Wei, Y. Shi, D. Fu, C. Jiang, L.W. Wang, F. Ren, Ion Irradiation inducing oxygen vacancy-rich NiO/NiFe(2) O(4) heterostructure for enhanced electrocatalytic water splitting, Small 17 (2021) e2103501.
[38] X. Chen, Z. Wang, S. Cao, X. Lin, C. Hao, X. Zhang, H. Chen, J. Wang, J. Liu, S. Liu, S. Wei, X. Lu, D. Sun, Steering elementary steps towards advanced alkaline hydrogen evolution via a sweet marriage of O-defected NiO and Cu, Appl. Catal. B Environ. Energy 357 (2024) 124295.
[39] Y. Da, Z. Tian, R. Jiang, G. Chen, Y. Liu, Y. Xiao, J. Zhang, S. Xi, W. Chen, X. Han, W. Hu, Single-atom pt doping induced p-type to n-type transition in NiO nanosheets toward self-gating modulated electrocatalytic hydrogen evolution reaction, ACS Nano 17 (2023) 18539–18547.
[40] T. Li, A. Fan, Y. Li, Y. Quo, Y. Zhu, H. Xie, Mn-Doped Tuned NiC/NiO heterostructure for efficient electron transfer in hydrogen evolution reaction, Adv. Energy Sustain. Res. (2025).
[41] L. Yan, J. Liang, D. Song, X. Li, H. Li, Modulation of charge redistribution in heterogeneous nio-ni3se4 nanosheet arrays for advanced water electrolysis, Adv. Funct. Mater. 34 (2023) 2308345.
[42] T. Jiang, X. Jiang, V. Kyriakou, K. Bouzek, H. Liao, Deep reconstruction of Ni–Al-based pre-catalysts for a highly efficient and durable anion-exchange membrane (AEM) electrolyzer, J. Mater. Chem. A 11 (2023) 26011.
[43] X. Jiang, V. Kyriakou, B. Wang, S. Deng, S. Costil, C. Chen, T. Liu, C. Deng, H. Liao, T. Jiang, Hierarchical microporous Ni-based electrodes enable "Two Birds with One Stone" in highly efficient and robust anion exchange membrane water electrolysis (AEMWE), Chem. Eng. J. 486 (2024) 150180.
[44] J. Lee, H. Jung, Y.S. Park, S. Woo, J. Yang, M.J. Jang, J. Jeong, N. Kwon, B. Lim, J. W. Han, S.M. Choi, High-efficiency anion-exchange membrane water electrolyzer enabled by ternary layered double hydroxide anode, Small 17 (2021) e2100639.
[45] V. Wang, N. Xu, J.-C. Liu, G. Tang, W.-T. Geng, VASPKIT: A user-friendly interface facilitating high-throughput computing and analysis using VASP code, Comput. Phys. Commun. 267 (2021) 108033.
[46] A. Al-Yunus, W. Al-Arjan, H. Traboulsi, R. Schuarca, P. Chando, I.D. Hosein, M. Hessien, Effect of Synthesis Conditions on CuO-NiO nanocomposites synthesized via saponin-green/microwave assisted-hydrothermal method, Nanomaterials 14 (2024) 308.
[47] H. Bishara, S. Lee, T. Brink, M. Ghidelli, G. Dehm, Understanding grain boundary electrical resistivity in Cu: the effect of boundary structure, ACS Nano 15 (2021) 16607–16615.
[48] M. Saber, C.C. Koch, R.O. Scattergood, Thermodynamic grain size stabilization models: an overview, Mater. Res. Lett. 3 (2015) 65–75.
[49] Y. Chen, Y. Liu, W. Zhai, H. Liu, T. Sakthivel, S. Guo, Z. Dai, Metastabilizing the ruthenium clusters by interfacial oxygen vacancies for boosted water splitting electrocatalysis, Adv. Energy Mater. 14 (2024) 2400059.
[50] M. Gong, W. Zhou, M.C. Tsai, J. Zhou, M. Guan, M.C. Lin, B. Zhang, Y. Hu, D. Y. Wang, J. Yang, S.J. Pennycook, B.J. Hwang, H. Dai, Nanoscale nickel oxide/nickel heterostructures for active hydrogen evolution electrocatalysis, Nat. Commun. 5 (2014) 4695.
[51] D. Yin, D. Chen, Y. Zhang, W. Wang, Q. Quan, W. Wang, Y. Meng, Z. Lai, Z. Yang, S. Yip, C.Y. Wong, X. Bu, X. Wang, J.C. Ho, Synergistic active phases of transition metal oxide heterostructures for highly efficient ammonia electrosynthesis, Adv. Funct. Mater. 33 (2023) 2303803.
[52] H. Wu, C. Chen, Nonaqueous Synthesis of Pd/PdO-Functionalized NiFe(2)O(4) nanoparticles enabled enhancing n-butanol detection, Nanomaterials 14 (2024) 1188.
[53] Y. Yao, D.W. Goodman, Direct evidence of hydrogen spillover from Ni to Cu on Ni–Cu bimetallic catalysts, J. Mol. Catal. A Chem. 383-384 (2014) 239–242.
[54] Q. Huang, F. Wang, Z. Sun, B. Zhang, W. Li, F. Guo, Y. Liu, F. Ren, X. Duan, In Situ growth and dynamic transformation of nickel chelate nanoarrays into reactive surface reconstituted heterostructure for overall water splitting, Adv. Funct. Mater. 34 (2024) 2407407.
[55] R. Jiang, J. Zhang, Y. Xie, L. Wu, S. Sun, P. Yu, E. Zhang, G. Wang, Construction of multiple heterogeneous interfaces boosting alkaline hydrogen evolution, Resour. Chem. Mater. 2 (2023) 253–261.
[56] F. Yuan, X. Wang, G. Liu, Y. Liu, Cu2S/NixSy multi-interfaces induced Ni(iii) for optimizing alkaline hydrogen evolution reaction, N. J. Chem. (2025).
[57] R. Solmaz, A. Döner, G. Kardaş, The stability of hydrogen evolution activity and corrosion behavior of NiCu coatings with long-term electrolysis in alkaline solution, Int. J. Hydrog. Energy 34 (2009) 2089–2094.
[58] M. Lykaki, E. Pachatouridou, S.A.C. Carabineiro, E. Iliopoulou, C. Andriopoulou, N. Kallithrakas-Kontos, S. Boghosian, M. Konsolakis, Ceria nanoparticles shape effects on the structural defects and surface chemistry: Implications in CO oxidation by Cu/CeO2 catalysts, Appl. Catal. B Environ. 230 (2018) 18–28.
[59] M. Konsolakis, The role of Copper–Ceria interactions in catalysis science: recent theoretical and experimental advances, Appl. Catal. B Environ. 198 (2016) 49–66.
[60] Y. Li, X. Tan, R.K. Hocking, X. Bo, H. Ren, B. Johannessen, S.C. Smith, C. Zhao, Implanting Ni-O-VOx sites into Cu-doped Ni for low-overpotential alkaline hydrogen evolution, Nat. Commun. 11 (2020) 2720.
[61] L. Huo, C. Jin, K. Jiang, Q. Bao, Z. Hu, J. Chu, Applications of nickel-based electrocatalysts for hydrogen evolution reaction, Adv. Energy Sustain. Res. 3 (2022) 2100189.
[62] G. Xu, J. Li, Y. Zeng, Z. Shi, W. Qi, K. Li, M. Xiao, C. Liu, W. Xing, J. Zhu, Synergy of Ni single atom and RuNi alloy nanocluster enables boosted hydrogen evolution at industrial current densities, Energy Environ. Sci. (2025).